ACS APPLIED ENERGY MATERIALS

www.acsaem.org Article

Stretchable and Self-Healing Thermally Chargeable Hybrid Supercapacitors for Low-Grade Waste-Heat Harvesting

Youngwoo Jo,† Anuja A. Yadav,† Seongjun Ko, Taewoong Park, Taewoo Lee, Chi Hwan Lee,* and Seok-Won Kang*

Cite This: *ACS Appl. Energy Mater.* 2026, 9, 10302−10313 Read Online

ACCESS | Metrics & More | Article Recommendations | Supporting Information

ABSTRACT: Thermally chargeable supercapacitors (TCSCs) have emerged as a promising platform for harvesting low-grade waste heat; however, their practical implementation remains limited by electrolyte dehydration, poor mechanical durability, and low energy output. Herein, we report a stretchable and self-healing thermally chargeable hybrid supercapacitor (TCHS) comprising a redox-active NiMn-layered double hydroxide (NiMn-LDH) electrode and a hydroxyl-rich PSSH/SOR/PVA solid polymer electrolyte. Incorporation of D-sorbitol establishes a dynamic hydrogen-bonding network that enhances water retention (>90% after 60 h) while providing high ionic conductivity (6.09 mS·cm^{-1}), autonomous self-healing (88% electrical recovery), and mechanical stretchability up to 350%. The hybrid thermal-charging mechanism combines ion-selective Soret diffusion within the electrolyte with redox-assisted thermoelectrochemical processes at the NiMn-LDH electrode. Under an applied temperature gradient, the hybrid device exhibits an ionic Seebeck coefficient of 2.06 mV·K^{-1}, representing a 21.18% enhancement compared with the symmetric NF//NF configuration (1.70 mV·K^{-1}). The enhanced thermoelectric response is attributed to the synergistic coupling of thermally driven ion migration and temperature-dependent interfacial redox processes. Under a temperature difference of 15 K, the device continuously harvested thermal energy and delivered a cumulative areal energy output of 8742 J·m^{-2} over 24 h, corresponding to a ∼29-fold improvement relative to the symmetric configuration. These findings demonstrate that integrating redox-active electrodes with mechanically robust polymer electrolytes provides an effective strategy for simultaneous thermal energy harvesting, charge storage, and flexible energy-conversion applications.

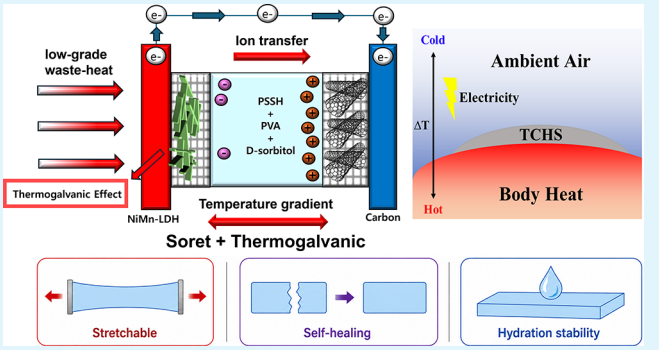

KEYWORDS: *NiMn-LDH electrode, Soret effect, self-healing, stretchability, thermally chargeable hybrid supercapacitor*

1. INTRODUCTION

The increasing demand for greenhouse reduction and energy efficiency enhancement has intensified interest in technologies capable of harvesting low-grade waste heat generated ubiquitously in industrial processes, electronic devices, and the human body; however, efficient conversion of low-grade heat (<100 °C) into usable electrical energy remains a major challenge.[1,2] Although conventional thermoelectric generators based on the electronic Seebeck effect have been extensively investigated, their practical deployment in low-temperature gradient conditions remains limited owing to intrinsically low Seebeck coefficients (typically on the order of tens of μV·K^{-1}), high thermal conductivity, and the mechanical properties of inorganic thermoelectric materials such as Bi_2Te_3, PbTe, and SiGe. These limitations restrict their applicability in flexible, lightweight, and real-world energy harvesting systems.[3−5]

To address these challenges, ionic thermoelectric systems have recently emerged as an alternative approach for low-grade heat-to-electric energy conversion.[6,7] In these systems, a temperature gradient induces directional ion migration via the Soret effect, resulting in ion accumulation and the generation of a thermally induced voltage.[8−13] Compared with electronic thermoelectric devices, ionic thermoelectric devices can exhibit Seebeck coefficients several orders of magnitude higher, typically in the mV·K^{-1} range, making them particularly appealing for low-temperature heat harvesting.[6,7] Recent studies have demonstrated substantial progress in ionic thermoelectric materials and device engineering, including polarized polymer electrolytes, redox-coupled thermogalvanic systems, and hybrid thermally chargeable architectures. These advances

Received: June 30, 2026
Revised: July 15, 2026
Accepted: July 17, 2026
Published: July 29, 2026

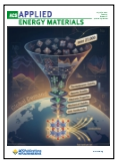

https://doi.org/10.1021/acsaem.6c02104
ACS Appl. Energy Mater. 2026, 9, 10302−10313

have highlighted that beyond electrolyte optimization, electrode design and interfacial redox engineering play equally important roles in improving ionic thermopower, accelerating charge-transfer kinetics, and enhancing thermal-to-electrical energy conversion efficiency.[14−17] Such findings strongly motivate the development of advanced redox-active electrodes capable of synergistically coupling ion-selective thermodiffusion with thermally responsive faradaic processes. Based on their dominant energy-conversion mechanism, ionic thermoelectric systems can generally be classified into three categories. The first category comprises Soret-driven ionic thermoelectric capacitors, where thermovoltage originates from ion-selective thermodiffusion under an applied thermal gradient, leading to concentration polarization. The second category includes thermoelectrochemical cells (thermogalvanic cells), in which entropy-driven redox reactions between thermally asymmetric electrodes generate electrical potential through temperature-dependent redox equilibrium shifts. More recently, hybrid thermally chargeable systems have emerged, integrating ionic thermodiffusion with interfacial redox-assisted thermoelectric conversion to enhance thermal-to-electrical energy harvesting efficiency. Unlike conventional thermogalvanic cells, which rely on dissolved redox couples in liquid electrolytes, these hybrid solid-state systems localize redox activity at the electrode/electrolyte interface, enabling improved mechanical stability, structural integration, and multifunctionality. This emerging hybrid strategy offers a promising pathway toward next-generation mechanically adaptive thermally chargeable energy-storage devices.[18−20]

Thermally chargeable supercapacitors (TCSCs) address this limitation by coupling thermal-energy conversion with electrochemical charge storage. Early TCSC studies primarily employed liquid electrolytes, wherein the thermally induced voltage originated solely from the Soret effect.[21,22] Although these systems demonstrate the fundamental feasibility of thermal charging, their practical application has been hindered by rapid power decay during discharge, relatively low energy density, potential electrolyte leakage, and limited environmental stability.[21−26] More recently, incorporation of redox-active electrodes has been proposed as an effective strategy to address these limitations. By coupling the Soret effect with temperature-sensitive redox processes at the electrode/electrolyte interface, enhanced thermoelectric performance has been proposed.[24−26] LDHs are attractive because their reversible transition-metal redox chemistry may contribute to temperature-dependent electrochemical potential while simultaneously providing high pseudocapacitive charge-storage capability.[24]

Although this approach improves energy density, considerations regarding mechanical and environmental stability of conventional electrolytes remain. Liquid electrolytes present inherent risks associated with leakage and evaporation, whereas solid electrolytes often exhibit fragility and low stretchability.[27] To bridge this gap, polymer-based electrolytes have emerged as a promising solution, offering mechanical flexibility, processability, and improved environmental tolerance.[28−33] However, achieving a balanced combination of high ionic conductivity, low thermal conductivity, mechanical stretchability, and long-term hydration stability within a single solid-state electrolyte remains challenging. Furthermore, the mechanical durability and damage tolerance, which are critical for real-world operation, are often overlooked in the design of TCSCs.

This study addresses these challenges by developing a thermally chargeable hybrid supercapacitor (TCHS) that combines ion-selective thermodiffusion with a redox-active electrode architecture. A battery-type NiMn-LDH electrode is integrated with a hydroxyl-rich PSSH/SOR/PVA electrolyte to enable efficient ionic transport under mechanical deformation. The performance of the proposed architecture is enabled by two key design features. First, D-sorbitol is incorporated to regulate the hydration environment of the polymer electrolyte through dynamic hydrogen-bonding interactions, thereby improving water retention, maintaining high ionic conductivity (6.09 $mS·cm^{-1}$), and enabling autonomous self-healing with 88% recovery. By combining stretchability with stable ionic transport, the PSSH/SOR/PVA electrolyte provides a mechanically resilient platform for thermally chargeable energy-storage devices, a capability that remains largely unexplored in previous TCSC systems. Second, the redox-active NiMn-LDH electrode may contribute temperature-dependent electrochemical processes in addition to ionic thermodiffusion, leading to an enhanced thermoelectric response. The hybrid device exhibits a Seebeck coefficient of 2.06 $mV·K^{-1}$, representing a 21.18% enhancement over the symmetric NF//NF configuration, corresponding to an areal energy output of 8742 $J·m^{-2}$ under a temperature difference of 15 K. These results demonstrate a promising strategy for integrating thermal-energy harvesting, electrochemical energy storage, and mechanical durability within a single solid-state platform for autonomous and wearable electronic systems.

2. METHODOLOGY

2.1. Materials and Characterization

Nickel nitrate hexahydrate ($Ni(NO_3)_2·6H_2O$, 98%), manganese nitrate tetrahydrate ($Mn(NO_3)_2·4H_2O$, 98%), urea (99%), poly(vinyl alcohol) (PVA, Mw 89,000–98,000, 99% hydrolyzed), poly(styrene sulfonic acid) (PSSH, 30 wt % in H_2O), and D-sorbitol (≥98%) were purchased from Sigma-Aldrich and used as received without further purification. Deionized water was used in all experiments.

The crystal structures of the NiMn-LDH electrodes were analyzed using X-ray diffraction (XRD, Malvern Panalytical). The surface morphology and microstructural features were examined employing field-emission scanning electron microscopy (FE-SEM, Hitachi). Electrochemical measurements, including CV, GCD, and EIS, were performed utilizing a Zive MP2A (WontATech) electrochemical workstation.

2.2. Preparation of Redox and Carbon Electrodes

The NiMn-LDH electrode was fabricated via simple hydrothermal synthesis using nickel foam as the current collector as shown in Scheme 1. Prior to synthesis, the nickel foam substrates were cleaned in hydrogen chloride, ethanol, and deionized water, followed by drying under 60 °C. $NiCl_2·6H_2O$ and $MnCl_2·4H_2O$ were dissolved in DIW with HMT and urea as hydrolysis agents to form a homogeneous solution. The cleaned Ni foam was immersed in the prepared solution and sealed within a Teflon-lined autoclave. The hydrothermal reaction was conducted at the 120 °C for 12 h to promote in situ growth of NiMn-LDH on the nickel foam surface. After the reaction, the obtained electrodes were thoroughly washed with DIW and ethanol and dried at 60 °C overnight. A carbon electrode was fabricated using TWCNT as the active material. The TWCNTs were mixed with carbon black and PvdF in a weight ratio of 8:1:1 using NMP solvent to form a uniform slurry. The slurry was coated on the nickel foam substrate and dried at 60 °C for 12 h to remove the solvent (Scheme 2).

https://doi.org/10.1021/acsaem.6c02104
ACS Appl. Energy Mater. 2026, 9, 10302−10313

Scheme 1. Synthesis of the NiMn-LDH Electrode

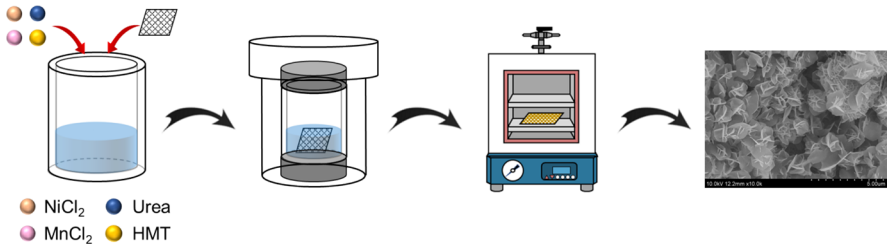

Scheme 2. Synthesis of the Carbon Electrode

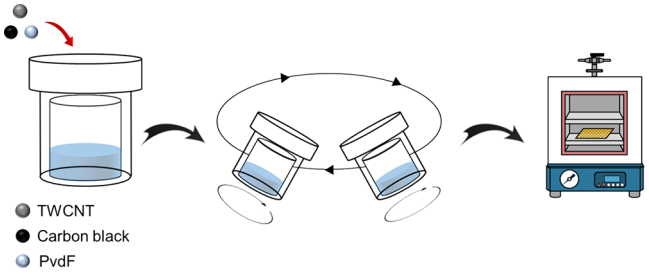

Subsequently, an oxygen plasma treatment (13.56 MHz, 100 W, 3 min) was applied to enhance the surface hydrophilicity.

2.3. Synthesis of Polymer Electrolyte

The polymer electrolyte was prepared by simultaneously stirring PSSH, PVA, and D-sorbitol in DIW at 80 °C under magnetic stirring. Fixed amounts of PSSH (11 g) and PVA (0.5 g) were employed, while the D-sorbitol content was varied relative to PSSH, corresponding to PSSH:D-sorbitol mass ratios of 10:1, 10:0.7, and 10:0.5, enabling systematic investigation of the influence of sorbitol content on electrolyte properties. The resulting electrolytes were denoted as SOR1, SOR0.7, and SOR0.5. All components were added concurrently into DIW and subjected to magnetic stirring at a constant temperature for 2 h until a homogeneous, transparent, orange solution was obtained. The resulting solution was cast into a rectangular mold and dried at 60 °C for 24 h to form polymer electrolyte. The fabrication process for electrolyte of the TCHS is illustrated in Scheme 3.

3. RESULTS AND DISCUSSION

3.1. Structural Characterization of the NiMn-LDH Electrode

The crystal structure of the synthesized NiMn-LDH electrode was investigated via X-ray diffraction (XRD) to confirm phase formation and layered characteristics. The diffraction pattern exhibits distinct diffraction peaks at 2θ values of 11.68°, 23.03°, 33.71°, 38.76°, 46.01°, 59.85°, and 61.05°, which correspond to the (003), (006), (101), (012), (015), (018), (110), and (113) crystallographic planes, respectively. These reflections closely align with PDF#38-0715, as shown in Figure 1a. The interlayer spacing was calculated from the (003) reflection using Bragg's law, where Cu Kα radiation (λ = 1.5406 Å) was used for the measurement.[34] From the 2θ value of 11.68°, the interlayer spacing was calculated to the 7.57 Å. This value closely aligns with previously reported value for NiMn-LDH structures, indicating that an expanded interlayer distance is advantageous for ion intercalation and transport.

The surface morphology and microstructural features of the NiMn-LDH electrode were observed employing FE-SEM. Figure 1b reveals that the electrode surface is uniformly covered with hydrotalcite-like structures, confirming the successful growth of NiMn-LDH on the substrate. The formation of the nanosheets is closely associated with the availability of carbonate ions (CO_3^{2-}) during the synthesis process.[35,36] Carbonate ions supplied from urea and HMT promote the rapid formation of layered double hydroxides, resulting in the formation of thin nanosheets. The aligned nanosheet structure formed via carbonate-assisted LDH growth is expected to enhance ion transport.

To investigate the surface elemental composition and chemical states of the synthesized NiMn-LDH electrode, X-ray photoelectron spectroscopy (XPS) analysis was performed. As shown in Figure 2a, the survey spectrum confirms the presence of Ni, Mn, O, and C elements, verifying the successful formation of the NiMn-LDH structure. The high-resolution Ni 2p spectrum (Figure 2b) was deconvoluted into two major spin–orbit doublets centered at approximately 853.9 and 871.7 eV and 855.2 and 873.2 eV, which are assigned to Ni^{2+} and Ni^{3+} species, respectively, accompanied by characteristic shake-up satellite peaks located at higher binding energies. The coexistence of Ni^{2+} and Ni^{3+} indicates mixed-valence nickel centers capable of participating in reversible Faradaic redox reactions. The Mn 2p spectrum (Figure 2c) exhibits multiple components corresponding to different manganese oxidation states, suggesting the presence of mixed-valence manganese species within the LDH framework. Such mixed oxidation states are commonly observed in NiMn-LDH materials and are beneficial for enhancing charge-transfer kinetics through synergistic redox interactions with nickel centers. The high-resolution O 1s spectrum (Figure 2d) can be deconvoluted into three components located at approximately 530.3, 531.0, and 531.8 eV, corresponding to lattice oxygen (M–O), hydroxyl groups (M–OH), and adsorbed oxygen/water species, respectively.[37] The dominant hydroxyl-related component confirms the successful formation of the hydroxide-rich layered structure. Collectively, the XPS results verify the successful synthesis of NiMn-LDH with mixed-valence transition-metal species and abundant hydroxyl functionalities, which are expected to facilitate reversible redox reactions and contribute to the enhanced electrochemical performance of the electrode.

The incorporation of Mn into the Ni-LDH lattice plays a crucial role in tuning the electrochemical and thermoelectric properties of the hybrid electrode. Mn introduces additional redox-active centers (Mn^{2+}/Mn^{3+}), alongside the intrinsic Ni^{2+}/Ni^{3+} couple, increasing the overall faradaic contribution and broadening the electrochemical activity window. Moreover, due to the larger ionic radius of Mn^{2+} compared

https://doi.org/10.1021/acsaem.6c02104
ACS Appl. Energy Mater. 2026, 9, 10302−10313

Scheme 3. Synthesis of PSSH/SOR/PVA Polymer Electrolyte

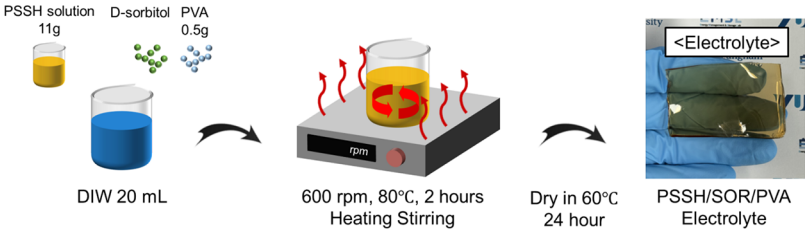

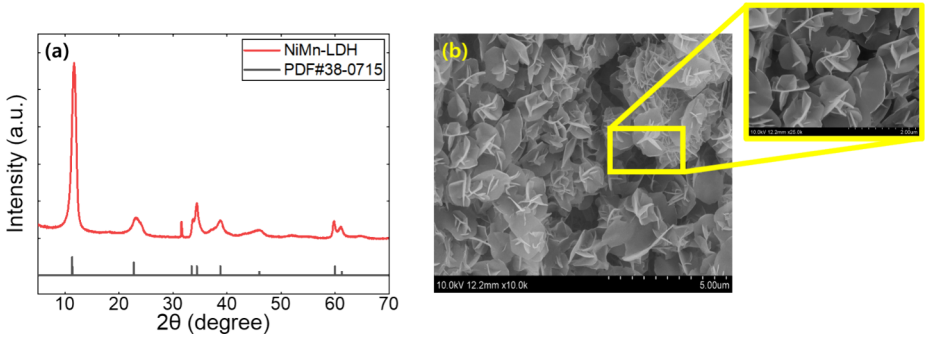

Figure 1. (a) XRD pattern of the NiMn-LDH consistent with PDF#38-0715, and (b) FE-SEM images of NiMn-LDH.

with Ni^{2+}, partial substitution induces lattice distortion and defect formation, which can increase the density of active sites and facilitate ion diffusion. The coexistence of dual redox centers also improves the temperature sensitivity of interfacial redox equilibria, which is beneficial for thermogalvanic-assisted charge generation under an applied thermal gradient.

3.2. Electrochemical Charge-Storage Properties of the NiMn-LDH Electrode

To decouple the charge-storage mechanisms that enable sustained thermal energy harvesting, the electrochemical behavior of the NiMn-LDH electrode was systematically evaluated. As shown in Figure 3a, the CV curves of the NiMn-LDH electrode recorded at scan rates of 5, 10, 20, and 40 mV/s within a potential window of 0–0.5 V (vs Ag/AgCl) exhibit pronounced redox peaks rather than a rectangular profile. Two distinct redox peaks are observed at 0.45 and 0.2 V, which can be attributed to the reversible redox transitions of Ni^{2+}/Ni^{3+} and Mn^{2+}/Mn^{3+} species within the layered double hydroxide structure.[38,39]

$$Ni(OH)_2 + OH^- \rightleftharpoons NiOOH + H_2O + e^- \quad (1)$$

$$MnO_2 + H_2O + e^- \rightleftharpoons MnOOH + OH^- \quad (2)$$

To quantitatively identify the charge-storage mechanism, the relationship between the peak current (i) and scan rate (v) was analyzed using the established power-law equation:[32]

$$i = i_{diff} + i_{cap} = av^b \quad (3)$$

$$\log(i) = \log(a) + b\cdot\log(v) \quad (4)$$

where b serves as an indicator of the dominant charge-storage process. Conventionally, a b-value of 0.5 corresponds to diffusion-controlled faradaic reactions, whereas a value of 1.0 indicates surface-controlled capacitive behavior. The calculated b-value of approximately 0.56 (Figure 3b) indicates that the electrochemical response of the NiMn-LDH electrode was predominantly governed by diffusion-controlled Faradaic reactions with an additional contribution from capacitive processes. This result is consistent with the battery-type characteristics of NiMn-LDH electrodes reported in previous studies.[38]

Following the CV analysis, the charge-storage capability of the NiMn-LDH was further evaluated via GCD measurements. As shown in Figure 3c, the GCD profiles exhibit clear nonlinearity and well-defined voltage plateaus rather than triangular shapes, which is characteristic of battery-type Faradaic charge storage behavior. This plateau is a critical performance indicator; it signifies that the electrode maintains a stable potential during the discharge phase, effectively acting as a redox reservoir that prevents the rapid voltage decay typically seen in carbon-based supercapacitors. Based on the GCD curves, the specific capacitance of the electrode was calculated using the following equations:[32,33]

$$C_s = \frac{i\cdot\Delta t}{\Delta V\cdot m} \quad (5)$$

where C_s ($F\cdot g^{-1}$) denotes specific capacitance, i (A) represents discharge current, Δt (s) represents discharge time, ΔV (V) denotes the voltage window, and m (g) is the mass of the active material. The energy and power densities were obtained from eqs 6 and 7, respectively.

$$E = \frac{C_s\cdot\Delta V^2}{2\cdot 3.6} \quad (6)$$

$$P = \frac{E}{\Delta t} \quad (7)$$

https://doi.org/10.1021/acsaem.6c02104
ACS Appl. Energy Mater. 2026, 9, 10302−10313

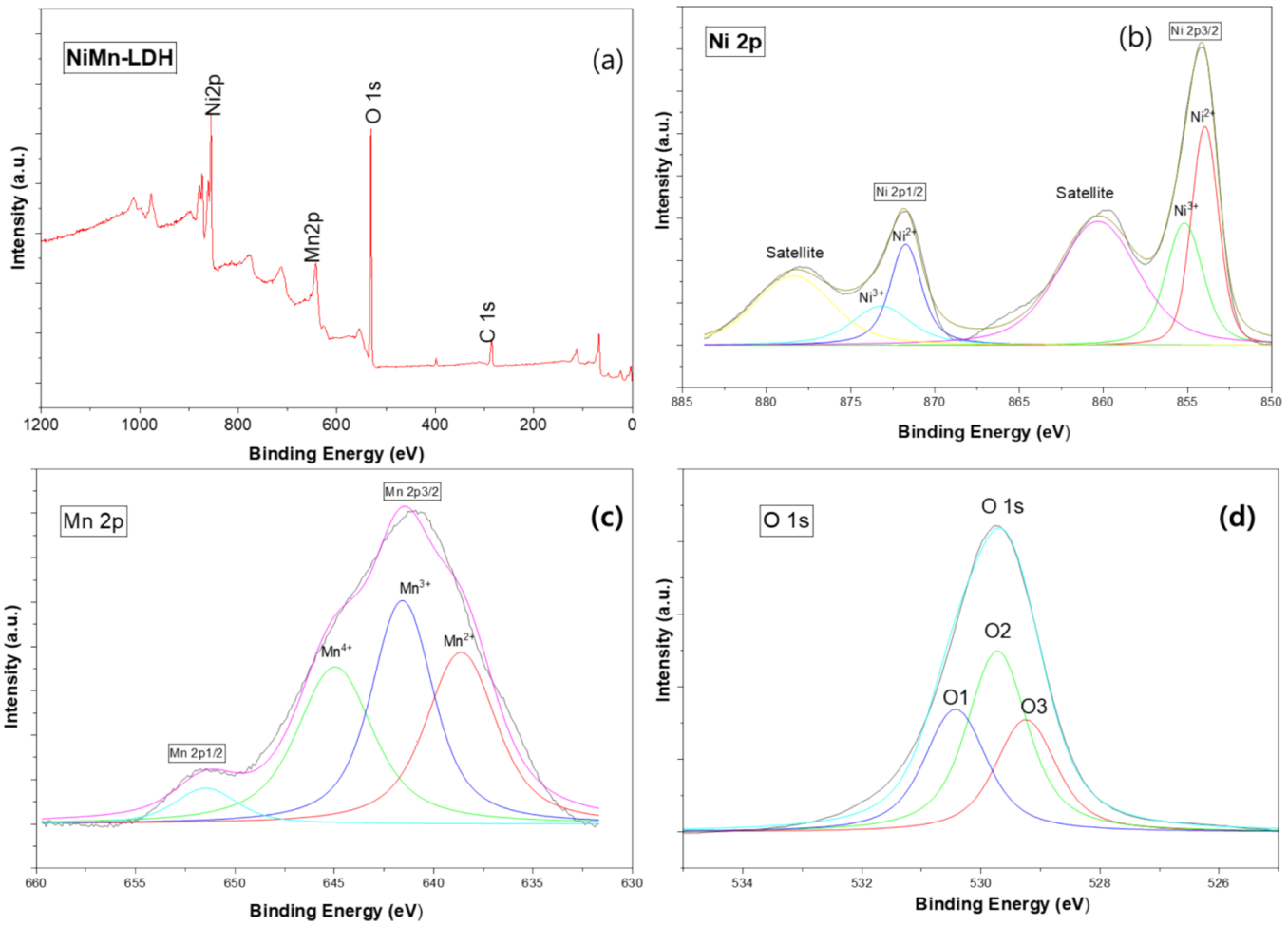

Figure 2. XPS spectra of the synthesized NiMn-LDH electrode: (a) survey scan, (b) Ni 2p spectrum, (c) Mn 2p spectrum, and (d) O 1s spectrum showing the chemical states of Ni, Mn, and O species.

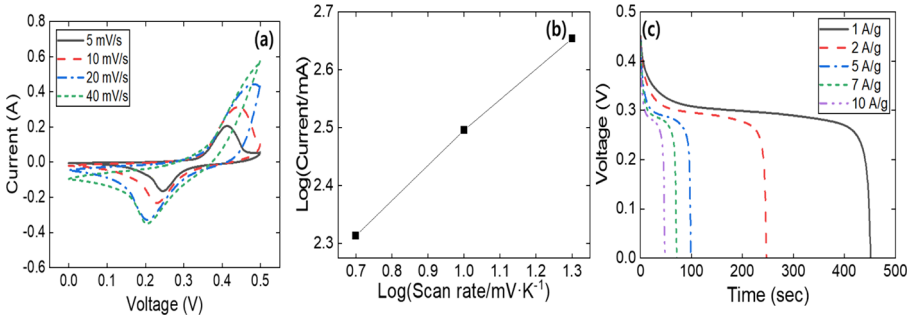

Figure 3. Electrochemical characterization of the NiMn-LDH electrode. (a) CV curves at multiple scan rates (5–40 mV/s), (b) log (i)–log(ν) plot derived from CV data, and (c) GCD profiles at multiple current densities.

where E (Wh·kg^{-1}) is the energy density and P (W·kg^{-1}) is the power density. The energy density was calculated from the GCD derived Cs using eq 6 within the applied potential window of 0–0.5 V vs Ag/AgCl. At a current density of 1 A·g^{-1}, the electrode delivered a high C_s of approximately 999 F·g^{-1}, yielding an energy density of 28.27 Wh·kg^{-1} and a power density of 0.26 kW·kg^{-1}. The combination of high Cs and stable discharge behavior confirms that the NiMn-LDH electrode provides the substantial charge storage necessary for sustaining energy accumulation during thermal charging. When integrated into the TCHS configuration, this redox-active reservoir enables the system to bridge the gap between transient thermal harvesting and permanent power delivery. Similarly, energy-storage performance has been benchmarked against previously reported NiMn-LDH and related layered double hydroxide-based supercapacitor systems (Table S1).

https://doi.org/10.1021/acsaem.6c02104
ACS Appl. Energy Mater. 2026, 9, 10302−10313

3.3. Ionic and Thermal Conductivity of the Polymer Electrolyte

The ionic transport properties of the PSSH/SOR/PVA electrolyte were evaluated employing EIS because ionic conductivity is a key parameter governing thermally driven ion diffusion in thermally charged systems. The bulk resistance was obtained from the high-frequency intercept of the Nyquist plot, as shown in Figure 4a, and the ionic conductivity was calculated using eq 8:[40,41]

$$\sigma = \frac{t}{R_b \cdot A} \tag{8}$$

where t (m) denotes electrolyte thickness, A (m^2) is the effective electrode–electrolyte contact area, and R_b (Ω) represents bulk resistance. As the D-sorbitol content increased, a gradual decrease in bulk resistance was observed, resulting in an overall increase in ionic conductivity. The optimized electrolyte composition exhibited a maximum ionic conductivity of 6.09 $m \cdot S^{-1}$ cm, which can be attributed to the increase in ionic conductivity and is attributed to the hydrophilic nature of sorbitol, which promotes water retention and facilitates the formation of continuous ionic conduction pathways within the polymer matrix. These interactions promote the effective dissociation and transport of mobile ions while maintaining a hydrated ionic conduction pathway within the polymer matrix.[42,43] The observed trend demonstrates that sorbitol incorporation effectively improves ionic transport within the electrolyte.

In addition to ionic conductivity, the thermal conductivity of the polymer electrolyte was evaluated because maintaining a stable temperature gradient across the device is essential for sustaining the Soret effect. Thermal conductivity was measured according to the ASTM D5470 standard, as shown in Figure S1. As the SOR content increased, the thermal conductivity of the electrolyte gradually increased linearly, as shown in Figure 4b. The optimized electrolyte exhibited a thermal conductivity of 0.46 $W \cdot m^{-1} \cdot K^{-1}$, which is marginally higher than that of the previously reported pristine PSSH film (~0.38 $W \cdot m^{-1} \cdot K^{-1}$).[30] This increase is attributed to the enhanced water content induced by the incorporation of SOR.[43] Despite this increase, the relatively low thermal conductivity remains advantageous for TCHS, as it suppresses heat dissipation across the electrolyte and is expected to help maintain the temperature gradient across the device during operation.

3.4. Structural Design and Functional Properties of the PSSH/SOR/PVA Electrolyte

The ternary polymer electrolyte was rationally designed by integrating three functionally distinct components to simultaneously achieve thermoelectric activity and mechanical adaptability. PSSH serves as the ion-selective thermodiffusive phase, where its sulfonic acid groups provide mobile protons (H^+) while the immobilized PSS^- backbone restricts anion migration, enabling proton-dominated Soret diffusion under an applied thermal gradient. PVA acts as the structural polymer scaffold owing to its excellent film-forming capability, flexibility, and hydroxyl-rich backbone, which stabilizes the electrolyte architecture and provides additional hydrogen-bonding sites. D-Sorbitol functions as a multifunctional plasticizer and dynamic hydrogen-bonding mediator; its abundant hydroxyl groups enhance polymer-chain mobility, improve water retention by increasing the bound-water fraction, and facilitate autonomous self-healing through reversible hydrogen-bond reconstruction. The synergistic integration of these three components is therefore essential for coupling efficient ionic thermodiffusion with mechanical resilience in the TCHS.[44,45]

3.4.1. Hydration Stability and Water Retention Behavior. Water retention capability was evaluated by monitoring the weight change of the electrolyte over time under ambient conditions (~25 °C) without external humidity controller. As shown in Figure 5a, the incorporation of SOR gradually improved water retention as SOR content increased. The optimized electrolyte (10 wt %, SOR) retained >90% of its initial weight after 60 h of exposure (~25 °C, ~70% RH). This improved water retention behavior can be attributed to the strong hydrogen-bonding interactions introduced by the SOR, which contains multiple hydroxyl groups capable of forming extensive hydrogen-bonding networks with water molecules. Within the sorbitol-modified polymer matrices, the improved water retention is consistent with stronger interactions between water molecules and the sorbitol-containing polymer network and enhanced stability under ambient conditions.[42−44] This behavior aligns with previous studies reporting that the incorporation of polyols, such as sorbitol, increases the fraction of bound water in polymer systems via extensive hydrogen bonding, thereby suppressing water evaporation.

In addition, the water-soluble nature of the electrolyte was visually confirmed, as shown in Figure 5b, wherein the electrolyte gradually dissolved in water over time. This behavior is a direct consequence of the highly hydrophilic polymer network and the absence of permanent chemical cross-linkers, highlighting the water-processable nature of the electrolyte and its potential compatibility with recyclable or transient electronic systems. While this solubility suggests sensitivity to moisture, the TCHS is designed for integration into hermetically encapsulated flexible devices. In this configuration, the high hydrophilicity is strategically leveraged to provide abundant hydrophilic sites that facilitate ionic transport. This molecular arrangement is expected to support efficient ion transport through the hydrated polymer network, yielding the high recorded ionic conductivity of 6.09 $mS \cdot cm^{-1}$ and ensuring operational stability under ambient thermal gradients.

3.4.2. Mechanical Resilience and Autonomous Self-Healing Kinetics. The mechanical stretchability of the PSSH/SOR/PVA electrolyte was quantitatively evaluated via tensile testing to assess its tolerance to mechanical deformation under practical operating conditions. Increasing the sorbitol content resulted in a pronounced increase in elongation at break, with the electrolyte containing sorbitol (10:1) exhibiting an elongation at break of approximately 350% (Figure 6a). This improvement is associated with the plasticizing effect of sorbitol, which enhances polymer-chain mobility within the polymer backbone induced by sorbitol incorporation. The multiple hydroxyl groups of sorbitol are involved in hydrogen-bond interactions with the sulfonic acid groups of PSSH, weakening rigid polymer–polymer interactions and enhancing segmental chain mobility.[45]

The self-healing capability of the polymer electrolyte was quantitatively examined by monitoring the recovery of the electrical resistance following mechanical cutting. After complete separation, the resistance rapidly increased to approximately

https://doi.org/10.1021/acsaem.6c02104
ACS Appl. Energy Mater. 2026, 9, 10302−10313

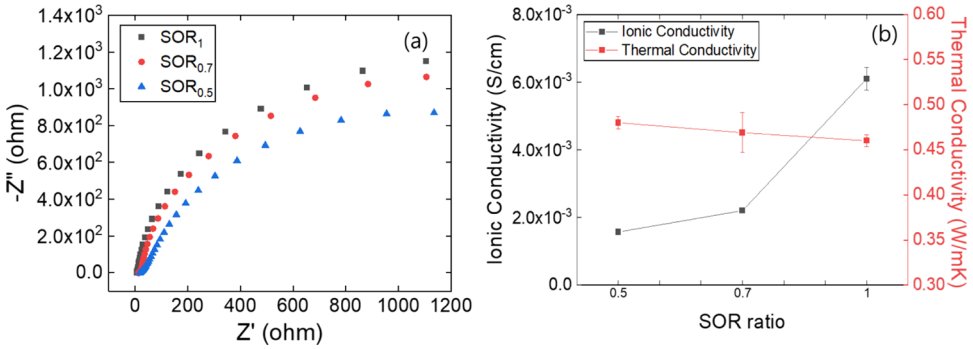

Figure 4. (a) Nyquist plots of PSSH/SOR/PVA electrolytes with different SOR contents. (b) Ionic conductivity and thermal conductivity as a function of SOR content.

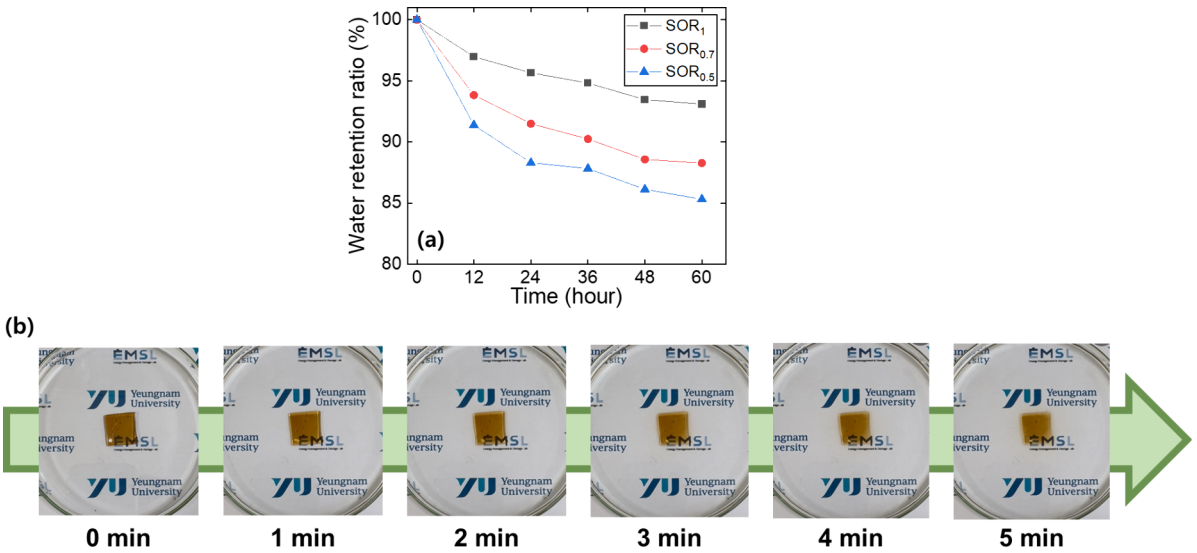

Figure 5. (a) Water retention behavior of electrolytes with different SOR contents under ambient conditions. (b) Images demonstrating the water-soluble behavior of the electrolyte upon exposure to water (1–5 min).

1.6×10^8 Ω, indicating complete electrical disconnection (Figure 6b). Following recontact of the cut interfaces, the resistance gradually decreased and recovered to approximately 86% of its original value without external stimuli. This recovery behavior is attributed to the spontaneous reconstruction of dynamic hydrogen bond networks within the polymer matrix.[43] The reversible interactions enabled molecular diffusion and interfacial re-association across the damaged regions, enabling partial restoration of ionic transport pathways after mechanical failure. In the proposed electrolyte system, the abundant hydroxyl groups of SOR and the sulfonic acid groups of PSSH were involved in the dynamic hydrogen-bond rearrangement at the cut interfaces. These interactions are believed to facilitate interfacial adhesion and molecular re-entanglement, resulting in the recovery of the continuous ionic conduction pathway.

In addition to electrical recovery, the self-healing behavior was visually confirmed, as the previously cut region of the electrolyte was observed to reconnect and regain a continuous morphology after re-connect, as shown in Figure 6c. These results indicate that the electrolyte can tolerate accidental mechanical damage, which is relevant for flexible or wearable thermally chargeable devices, rather than for structural load-bearing applications.

3.5. Thermoelectric Performance Evaluation

3.5.1. Device Configuration and Thermal Charging Process. The TCHS was fabricated in a planar configuration, comprising a hydroxyl-rich solid polymer electrolyte (SOR1) layer positioned between two asymmetric electrodes; NiMn-LDH electrode on the hot side and a carbon electrode on the cold side. The electrolyte area was fixed at 3×3 cm^2, and the electrode–electrolyte contact area was controlled at 1×3 cm^2. To impose a controlled temperature gradient across the device, a commercial Peltier module (TEC 1-12706) was placed under the electrolyte layer as shown in Figure 7a,b. All thermal charging experiments were conducted under 25 °C and 70% relative humidity. The cold-side temperature was fixed at 20 °C, whereas the hot-side temperature was sequentially set to 30, 35, and 40 °C, corresponding to applied temperature differences (ΔT) of 10, 15, and 20 K, respectively.

3.5.2. TCHS Device Performance. Thermoelectric performance was initially evaluated using a symmetric NF//NF configuration as a reference system, wherein identical nickel foam electrodes were positioned on both the hot and cold sides. In this configuration, the generated thermal voltage was solely governed by the Soret effect within the polymer electrolyte. Owing to the

https://doi.org/10.1021/acsaem.6c02104
ACS Appl. Energy Mater. 2026, 9, 10302–10313

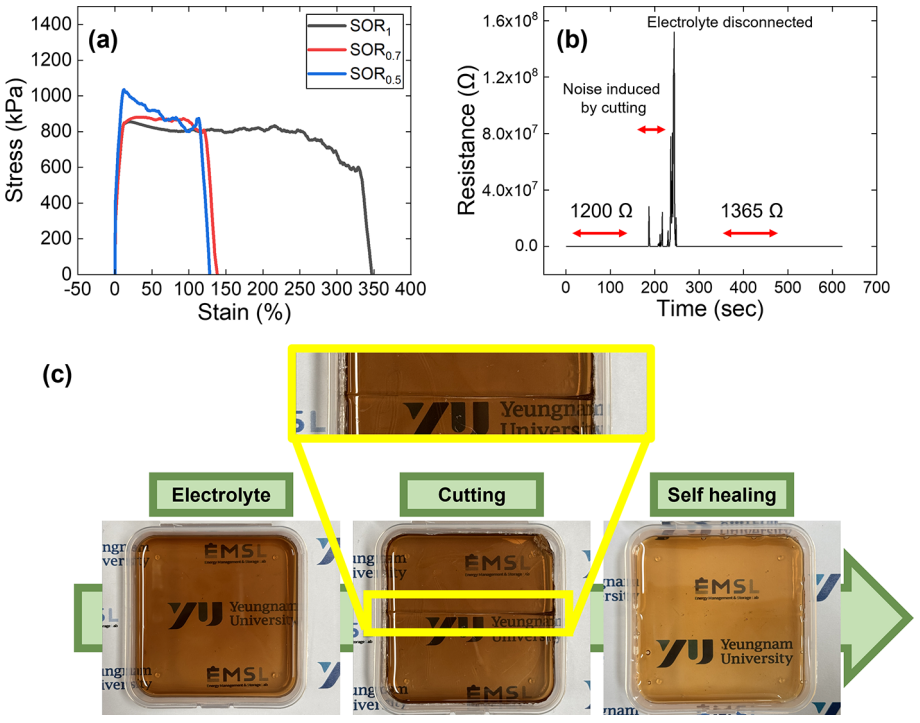

Figure 6. (a) Stress–strain curves of electrolytes with different SOR contents. (b) Resistance change during cutting and self-healing process. (c) Actual photograph demonstrating the self-healing behavior of the electrolyte after mechanical damage.

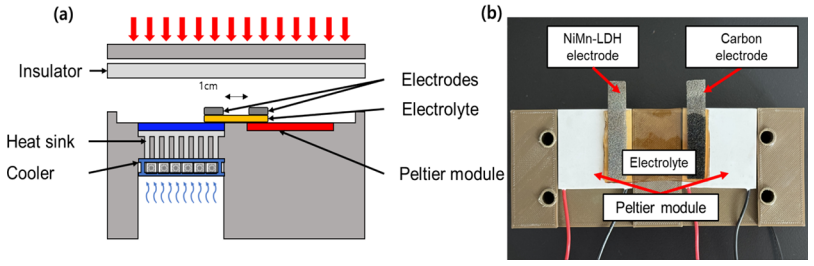

Figure 7. (a) Schematic of the custom-device used for evaluating the thermoelectric performance of TCHS. (b) Photograph of assembled device showing NiMn-LDH//carbon systems.

structural characteristics of PSSH, sulfonated PSS possesses a high molecular weight and is effectively immobilized within the polymer matrix such that proton thermos-diffusion becomes the dominant ionic transport process under the applied thermal gradient. Consequently, a relatively low Seebeck coefficient was obtained compared with that of the hybrid configuration, representing the baseline thermoelectric response.

Subsequently, the thermoelectric performance was investigated utilizing a hybrid electrode configuration, wherein a NiMn-LDH electrode was introduced on the hot side and a carbon-based electrode was placed on the cold side. As shown in Figure 8a, under an applied temperature difference of 10, 15, and 20 K, the symmetric NF//NF configuration exhibited a Seebeck coefficient of approximately 1.70 mV·K^{-1}, reflecting a predominantly Soret-driven thermoelectric response. By contrast, the hybrid NiMn-LDH//carbon configuration achieved an increased Seebeck coefficient of ∼2.06 mV·K^{-1} (Figure 8b), representing a 21.18% enhancement. Also, the observed increase in the Seebeck coefficient was attributed to an additional thermogalvanic contribution (α_{tg}) arising from the redox-active NiMn-LDH electrode (Figure 8c).[43,44] The extended charging duration reflects the hybrid configuration enabled the coupling of Soret-driven ion migration with redox-mediated thermoelectric conversion at the hot-side electrode/electrolyte interface. Similar hybrid thermos-electrochemical behavior involving coupled ionic thermos-diffusion and temperature-dependent redox processes has also been discussed in previous thermos-galvanic and thermos-electrochemical studies.[45−47]

$$\alpha_{hybrid} = \alpha_{Soret} + \alpha_{tg} \tag{9}$$

where α_{Soret} originates from ion-selective thermodiffusion within the polymer electrolyte and α_{tg} represents the additional thermogalvanic contribution associated with temperature-dependent redox equilibria at the NiMn-LDH electrode/electrolyte interface. To further explain the thermogalvanic contribution of the NiMn-LDH electrode, the enhanced thermoelectrochemical response is likely associated with temperature-dependent Ni/Mn redox equilibria occurring at the electrode/electrolyte

https://doi.org/10.1021/acsaem.6c02104
ACS Appl. Energy Mater. 2026, 9, 10302−10313

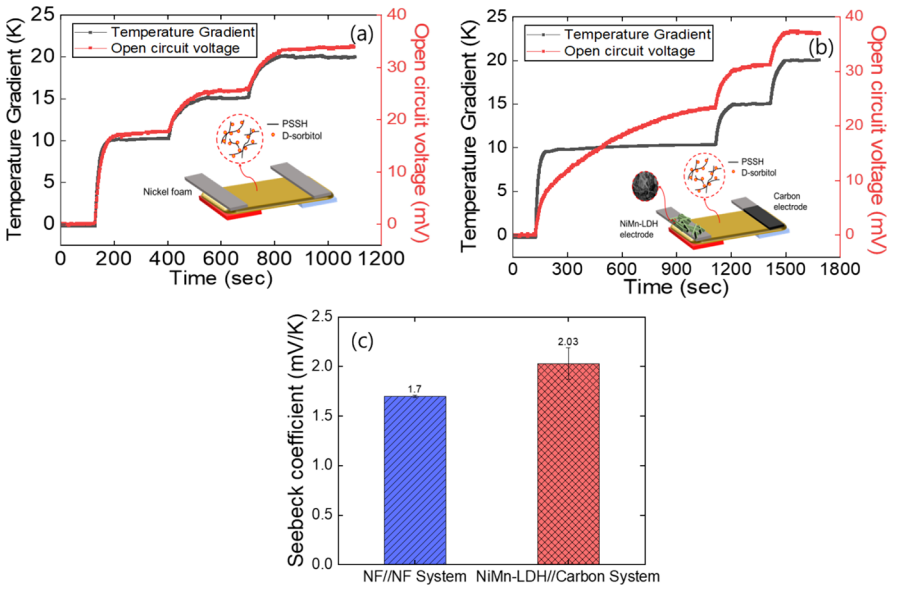

Figure 8. (a, b) Open-circuit voltage responses under stepwise temperature gradients for the NiMn-LDH//carbon system and the NF//NF system. (c) Comparison of Seebeck coefficient between the two systems.

interface under alkaline conditions. Specifically, Ni-based species undergo reversible oxidation according to eq 1, while Mn-associated species may contribute through temperature-dependent redox transitions described in eq 2. Because these redox equilibria are thermally activated, the imposed temperature gradient can shift the electrochemical equilibrium at the electrode/electrolyte interface, thereby potentially generating an additional thermogalvanic contribution beyond the Soret-driven ionic thermodiffusion process. Consequently, the hybrid configuration produces a higher Seebeck coefficient than the symmetric NF//NF system. As shown in Figure 8b, the hybrid configuration exhibited a delayed and gradual voltage increase compared with the symmetric NF//NF configuration, particularly in the low-temperature-gradient region. In the symmetric configuration, a nearly immediate voltage response was observed following application of the temperature gradient, consistent with a predominantly Soret-driven response. By contrast, the slower voltage evolution observed in the hybrid system is likely associated with the coupled processes of proton thermodiffusion and gradual electrochemical equilibration at the electrode/electrolyte interface. Furthermore, energy-storage capability under thermal charging conditions was evaluated. The output energy density was measured under a fixed temperature gradient of 15 K with an external load of 1 kΩ.

As shown in Figure S2a,b, the TCHS exhibited a continuous increase in cumulative electrical energy output during thermal charging, indicating sustained conversion of low-grade thermal energy into electrical energy through coupled Soret-driven ion thermodiffusion and redox-assisted charge accumulation at the NiMn-LDH electrode. After 24 h of operation under a constant temperature gradient of 15 K, the hybrid TCHS delivered a cumulative electrical energy output of 2.62 J, corresponding to an areal energy output of 8742 J·m^{-2} based on the active electrode–electrolyte contact area (3 cm^2). The reported areal energy output represents the cumulative electrical energy delivered to an external load during continuous thermal charging rather than the instantaneous electrochemical energy stored within the device. Considering the planar device architecture and intended surface-mounted operation, cumulative areal energy output was selected as the primary metric for performance comparison. The gradual increase in harvested energy reflects the continuous yet low-power nature of low-grade thermal energy harvesting, where small temperature differences are maintained over extended periods. Under identical conditions, the symmetric NF//NF device delivered a substantially lower areal energy output of 301.5 J·m^{-2}. The superior performance of the hybrid configuration is attributed to the synergistic contributions of Soret-driven ion thermodiffusion within the electrolyte and redox-assisted charge storage provided by the NiMn-LDH electrode.[48,49] To evaluate the practical significance of the present TCHS, a performance comparison with recently reported thermally chargeable supercapacitors and ionic thermoelectric systems is summarized in Table S2 included in the Supporting Information. The present device demonstrates competitive thermopower and superior cumulative areal energy output under a relatively low thermal gradient (ΔT = 15 K), highlighting the effectiveness of coupling Soret-driven ion thermodiffusion with interfacial redox-assisted thermogalvanic processes.

3.5.3. TCHS Working Mechanism. The TCHS operates through a three-stage cycle consisting of thermal charging, electrical discharging, and relaxation, as illustrated in Figure 9a. During thermal charging, application of a temperature gradient induces directional ion migration within the electrolyte, resulting in ion accumulation near the cold side and the generation of a thermovoltage across the device. The generated thermovoltage can be approximated as[7,25,50–52]

$$V_{th} = \alpha \Delta T \tag{9}$$

where V_{th} is the thermally generated voltage, α is the ionic Seebeck coefficient, and ΔT is the applied temperature difference. The instantaneous electrical power delivered to an

https://doi.org/10.1021/acsaem.6c02104
ACS Appl. Energy Mater. 2026, 9, 10302−10313

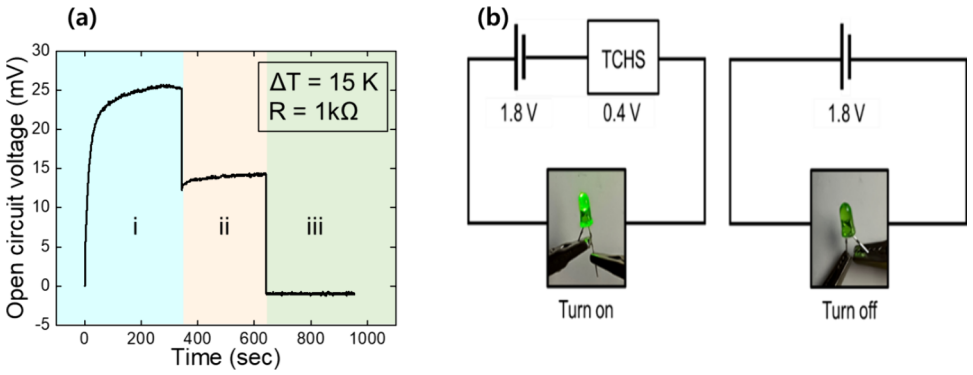

Figure 9. (a) Working mode under applied temperature gradient (ΔT = 15 K and 1 kΩ). (b) Practical demonstration of LED operation using a TCHS as auxiliary power. "For Table of Contents Only"

external load is given by

$$P(t) = \frac{V(t)^2}{R} \tag{11}$$

and the cumulative electrical energy harvested during thermal charging is obtained by

$$E = \int_0^t \frac{V(t)^2}{R} dt \tag{12}$$

The corresponding areal energy output was calculated using

$$E_A = \frac{1}{AR} \int_0^t V(t)^2 dt \tag{13}$$

where A is the active electrode-electrolyte contact area and R is the external load resistance.

Following removal of the temperature gradient, the device enters the relaxation stage, during which ionic redistribution restores the initial equilibrium state. In addition, practical operation of the TCHS was demonstrated by powering an LED through a series connection in conjunction with an external 1.8 V power supply, as shown in Figure 9b. The LED was successfully illuminated by the combined voltage contribution from the thermally charged TCHS and the external source. The LED illumination experiment qualitatively demonstrates that the thermally charged TCHS contributes supplementary voltage to the external circuit. Although the TCHS alone was insufficient to directly power the LED, its addition increased the total circuit voltage and enabled LED operation under the tested conditions. These results indicate that the TCHS can function as an auxiliary power source capable of supplementing low-power electronic systems using harvested thermal energy. These results demonstrate that the TCHS functions as an auxiliary power source capable of supplying supplementary electrical energy harvested from low-grade thermal inputs.

4. CONCLUSIONS

In this study, we develop a stretchable and self-healing thermally chargeable hybrid supercapacitor (TCHS) capable of efficient energy harvesting under a low-grade thermal gradient for practical applications. By integrating a battery-type electrode, NiMn-LDH, at the hot side with a hydroxyl-rich polymer electrolyte, the device demonstrated an enhanced ionic Seebeck coefficient of approximately 2.06 mV·K^{-1}, representing a 21.18% increase compared with the symmetric configuration (~1.70 mV·K^{-1}). This enhancement is attributed to the synergistic coupling of ion-selective Soret diffusion and temperature-dependent interfacial redox processes at the NiMn-LDH electrode. The optimized polymer electrolyte exhibited an ionic conductivity of 6.09 mS·cm^{-1} and a low thermal conductivity of 0.46 W·m^{-1}·K^{-1}, supporting stable Soret-driven ion transport. The extensive hydrogen bonding induced by sorbitol increased the fraction of bound water, resulting in excellent water retention (>90% after 60 h) under ambient conditions. In addition, a high stretchability (~350%), self-healing capability (~86% resistance recovery), and water solubility were achieved, demonstrating its suitability for practical applications. Practical device applicability was validated by integrating the TCHS in series with an external power source to successfully operate an LED, confirming its role as an auxiliary thermal energy-harvesting unit. These findings establish a promising strategy for integrating mechanically adaptive thermally chargeable systems into wearable and self-powered low-energy electronics. Future studies will focus on evaluating thermoelectric performance under dynamic mechanical deformation and extended thermal cycling to further validate long-term device reliability.

■ ASSOCIATED CONTENT

Data Availability Statement

Data will be made available on request.

Supporting Information

The Supporting Information is available free of charge at https://pubs.acs.org/doi/10.1021/acsaem.6c02104.

Design and performance of the thermally chargeable hybrid supercapacitors; experimental setup and measurement configuration for evaluating thermal conductivity, based on an ASTM D5470 method, described to verify low heat transport characteristics required for maintaining a temperature gradient between electrodes; energy harvesting behavior under a temperature gradient (ΔT = 15 K, 1 kΩ) presented for both symmetric and asymmetric configurations, demonstrating the enhanced areal energy output of the NiMn-LDH//carbon system; comparative analyses with previously reported NiMn-LDH-based asymmetric supercapacitors provided to

https://doi.org/10.1021/acsaem.6c02104
ACS Appl. Energy Mater. 2026, 9, 10302−10313

benchmark electrochemical energy and power performance, while comparisons with thermally chargeable supercapacitors and ionic thermoelectric energy storage systems are included to contextualize the thermally driven energy harvesting capability (PDF)

AUTHOR INFORMATION

Corresponding Authors

Chi Hwan Lee – *Weldon School of Biomedical Engineering, Purdue University, West Lafayette, Indiana 47907, United States; Schools of Mechanical Engineering, Materials Engineering, and Electrical and Computer Engineering, Purdue University, West Lafayette, Indiana 47907, United States;* orcid.org/0000-0002-4868-7054; Email: lee2270@purdue.edu

Seok-Won Kang – *Department of Automotive Engineering, Yeungnam University, 280 Daehak-ro, Gyeongsan, Gyeongbuk 38541, Republic of Korea;* orcid.org/0000-0003-2062-5297; Email: swkang@yu.ac.kr

Authors

Youngwoo Jo – *Department of Automotive Engineering, Yeungnam University, 280 Daehak-ro, Gyeongsan, Gyeongbuk 38541, Republic of Korea*

Anuja A. Yadav – *Department of Automotive Engineering, Yeungnam University, 280 Daehak-ro, Gyeongsan, Gyeongbuk 38541, Republic of Korea; Faculty of Pure and Applied Sciences, University of Tsukuba, 1-1-1 Tennodai, Tsukuba, Ibaraki 305-8573, Japan;* orcid.org/0000-0001-7823-1966

Seongjun Ko – *Department of Automotive Engineering, Yeungnam University, 280 Daehak-ro, Gyeongsan, Gyeongbuk 38541, Republic of Korea*

Taewoong Park – *Weldon School of Biomedical Engineering, Purdue University, West Lafayette, Indiana 47907, United States*

Taewoo Lee – *Department of Automotive Engineering, Yeungnam University, 280 Daehak-ro, Gyeongsan, Gyeongbuk 38541, Republic of Korea*

Complete contact information is available at: https://pubs.acs.org/doi/10.1021/acsaem.6c02104

Author Contributions

†Youngwoo Jo and Anuja A. Yadav contributed equally to this work. **Youngwoo Jo**: formal analysis, data curation, investigation, visualization, and writing—original draft. **Anuja A. Yadav**: formal analysis, methodology, investigation, and writing—original draft. **Seongjun Ko**: data curation, investigation, and writing—original draft. **Taewoong Park**: investigation and writing—original draft. **Taewoo Lee**: investigation and writing—original draft. **Chi Hwan Lee**: formal analysis, resources, and writing—review and editing. **Seok-Won Kang**: formal analysis, conceptualization, funding acquisition, methodology, project administration, supervision, and writing—review & editing.

Notes

The authors declare no competing financial interest.

ACKNOWLEDGMENTS

This work was supported by the National Research Foundation of Korea (NRF) grant funded by the Korea government (MSIT) (No. RS-2025-16066656). The author acknowledges Purdue University for granting permission for the sabbatical stay of S.-W. Kang.

REFERENCES

(1) Simonetti, R.; Molinaroli, L.; Manzolini, G. Experimental and Analytical Study of an Innovative Integrated Dual-Source Evaporator for Solar-Assisted Heat Pumps. *Sol. Energy* **2019**, *194*, 939–951.

(2) Maye, S.; Girault, H. H.; Peljo, P. Thermally Regenerative Copper Nanoslurry Flow Batteries for Heat-to-Power Conversion with Low-Grade Thermal Energy. *Energy & Environ. Sci.* **2020**, *13*, 2191–2199.

(3) Tang, X.; Li, Z.; Liu, W.; Zhang, Q.; Uher, C. A Comprehensive Review on Bi_2Te_3-Based Thin Films: Thermoelectrics and Beyond. *Interdiscip. Mater.* **2022**, *1*, 88–115.

(4) Chen, Y.; Hou, X.; Ma, C.; Dou, Y.; Wu, W. Review of Development Status of Bi_2Te_3-Based Semiconductor Thermoelectric Power Generation. *Adv. Mater. Sci. Eng.* **2018**, *2018*, No. 1210562.

(5) Ruvinskii, M. A.; Kostyuk, O. B.; Dzundza, B. S. The Influence of the Size Effects on the Termoelectric Properties of PbTe Thin Films. *J. Nano- Electron. Phys.* **2016**, *8*, No. 02051.

(6) Verma, S.; Padha, B.; Ahmed, A.; Singh, R.; Dubal, D. P.; Arya, S. Thermoelectric Supercapacitors: Materials, Challenges and Future Outlook. *Prog. Energy* **2024**, *6*, No. 042002.

(7) Al-Zubaidi, A.; Ji, X.; Yu, J. Thermal Charging of Supercapacitors: A Perspective. *Sustainable Energy Fuels* **2017**, *1*, 1457–1474.

(8) Wang, H.; Li, W.; Xu, X.; Jiang, J.; Huang, Y.; Fang, G. In Situ Photocatalytically Enhanced Thermogalvanic Cells for Electricity and Hydrogen Production. *Science* **2023**, *381*, 291–296.

(9) Wang, H.; Xu, X.; Wang, H.; Li, W.; Huang, Y.; Jiang, J.; Jing, M.; Bai, Y.; Fang, G. High-Thermopower Polarized Electrolytes Enabled by Methylcellulose for Low-Grade Heat Harvesting. *Sci. Adv.* **2022**, *8*, No. eabl5318.

(10) Bai, F.; Miao, L.; Wang, C.; Xie, Y.; Chen, J.; Zhou, J. Thermosensitive Crystallization-Boosted Liquid Thermocells for Low-Grade Heat Harvesting. *Science* **2020**, *370*, 342–346.

(11) Mageeth, A. M. A.; Park, S.; Jeong, M.; Kim, W.; Yu, C. Planar-Type Thermally Chargeable Supercapacitor without an Effective Heat Sink and Performance Variations with Layer Thickness and Operation Conditions. *Appl. Energy* **2020**, *268*, No. 114975.

(12) Lim, H.; Shi, Y.; Qiao, Y. Thermally Chargeable Supercapacitor based on Nickel-Coated Nanoporous Carbon. *Int. J. Green Energy* **2018**, *15*, 53–56.

(13) Lee, S. W.; Yang, Y.; Lee, H.; Ghasemi, H.; Kraemer, D.; Chen, G.; Cui, Y. An Electrochemical System for Efficiently Harvesting Low-Grade Heat Energy. *Nat. Commun.* **2014**, *5*, No. 3942.

(14) Jung, S.-M.; Kang, S.-Y.; Lee, B.-J.; Lee, J.; Kwon, J.; Lee, D.; Kim, Y.-T. Fe–N–C Electrocatalyst for Enhancing Fe(II)/Fe(III) Redox Kinetics in Thermo-Electrochemical Cells. *Adv. Funct. Mater.* **2023**, *33*, No. 2304067.

(15) Yu, B.; Xiao, H.; Zeng, Y.; Liu, S.; Wu, D.; Liu, P.; Guo, J.; Xie, W.; Duan, J.; Zhou, J. Cost-Effective n-Type Thermocells Enabled by Thermosensitive Crystallizations and 3D Multi-Structured Electrodes. *Nano Energy* **2022**, *93*, No. 106795.

(16) Jung, S.-M.; Kwon, J.; Lee, J.; Han, I. K.; Kim, K.-S.; Kim, Y. S.; Kim, Y.-T. Cost-Efficient Nickel-Based Thermo-Electrochemical Cells for Utilizing Low-Grade Thermal Energy. *J. Power Sources* **2021**, *494*, No. 229705.

(17) Jung, S.-M.; Kwon, J.; Lee, J.; Lee, B.-J.; Kim, K.-S.; Yu, D.-S.; Kim, Y.-T. Hybrid Thermo-Electrochemical Energy Harvesters for Conversion of Low-Grade Thermal Energy into Electricity via Tungsten Electrodes. *Appl. Energy* **2021**, *299*, No. 117334.

(18) Härtel, A.; Janssen, M.; Weingarth, D.; Presser, V.; Van Roij, R. Heat-to-Current Conversion of Low-Grade Heat from a Thermocapacitive Cycle by Supercapacitors. *Energy Environ. Sci.* **2015**, *8*, 2396–2401.
(19) Wang, J.; Feng, S.; Yang, Y.; Hau, N. Y.; Munro, M.; Ferreira-Yang, E.; Chen, G. Thermal Charging Phenomenon in Electrical Double Layer Capacitors. *Nano Lett.* **2015**, *15*, 5784–5790.
(20) Platten, J. K. The Soret Effect: A Review of Recent Experimental Results. *J. Appl. Mech.* **2006**, *91*, No. 153102.
(21) Qiao, Y.; Punyamurtula, V. K.; Han, A. Thermally Induced Capacitive Effect of a Nanoporous Monel. *Appl. Phys. Lett.* **2007**, *91*, No. 153102.
(22) Lim, H.; Lu, W.; Chen, X.; Qiao, Y. Effects of Ion Concentration on Thermally-Chargeable Double-Layer Supercapacitors. *Nanotechnology* **2013**, *24*, No. 465401.
(23) Bonetti, M.; Nakamae, S.; Huang, B. T.; Salez, T. J.; Wiertel-Gasquet, C.; Roger, M. Thermoelectric Energy Recovery at Ionic-Liquid/Electrode Interface. *J. Chem. Phys.* **2015**, *142*, No. 244708.
(24) Shao, M.; Zhang, R.; Li, Z.; Wei, M.; Evans, D. G.; Duan, X. Layered Double Hydroxides toward Electrochemical Energy Storage and Conversion: Design, Synthesis and Applications. *Chem. Commun.* **2015**, *51*, 15880–15893.
(25) Quickenden, T. I.; Mua, Y. A Review of Power Generation in Aqueous Thermogalvanic Cells. *J. Electrochem. Soc.* **1995**, *142* (11), 3985–3994.
(26) Gunawan, A.; Lin, C.; Buttry, D. A.; Mujica, V.; Taylor, R. A.; Prasher, R. S.; Phelan, P. E. Liquid Thermoelectrics: Review of Recent and Limited New Data of Thermogalvanic Cell Experiments. *Nanoscale Microscale Thermophys. Eng.* **2013**, *17*, 304–323.
(27) Jiang, K.; Jia, J.; Chen, Y.; Li, L.; Wu, C.; Zhao, P.; Zhu, D. Y.; Zeng, W. An Ionic Thermoelectric Generator with a Giant Output Power Density and High Energy Density Enabled by Synergy of Thermodiffusion Effect and Redox Reaction on Electrodes. *Adv. Energy Mater.* **2023**, *13*, No. 2204357.
(28) He, H.; Zhang, L.; Yue, S.; Yu, S.; Wei, J.; Ouyang, J. Enhancement in the Mechanical Stretchability of PEDOT: PSS Films by Compounds of Multiple Hydroxyl Groups for Their Application as Transparent Stretchable Conductors. *Macromolecules* **2021**, *54*, 1234–1242.
(29) Ying, C.; Chen, Y.; Yang, H.; Mariotti, D.; Bo, Z. Regulation of Electrode–Electrolyte Interactions for Improved Heat Recovery of a Thermo-Induced Electric Double-Layer Capacitor. *Energy Fuels* **2022**, *36*, 3304–3312.
(30) Kim, S. L.; Lin, H. T.; Yu, C. Thermally Chargeable Solid-State Supercapacitor. *Adv. Energy Mater.* **2016**, *6*, No. 1600546.
(31) Kumar, J.; Neiber, R. R.; Abbas, Z.; Soomro, R. A.; BaQais, A.; Amin, M. A.; El-Bahy, Z. M. Hierarchical NiMn-LDH Hollow Spheres as a Promising Pseudocapacitive Electrode for Supercapacitor Application. *Micromachines* **2023**, *14*, No. 487.
(32) Noori, A.; El-Kady, M. F.; Rahmanifar, M. S.; Kaner, R. B.; Mousavi, M. F. Towards Establishing Standard Performance Metrics for Batteries, Supercapacitors and Beyond. *Chem. Soc. Rev.* **2019**, *48*, 1272–1341.
(33) Roldán, S.; Barreda, D.; Granda, M.; Menéndez, R.; Santamaría, R.; Blanco, C. An Approach to Classification and Capacitance Expressions in Electrochemical Capacitors Technology. *Phys. Chem. Chem. Phys.* **2015**, *17*, 1084–1092.
(34) Chen, S.; Lu, C.; Liu, L.; Xu, M.; Wang, J.; Deng, Q.; Zeng, Z.; Deng, S. A Hierarchical Glucose-Intercalated NiMn-G-LDH@$NiCo_2S_4$ Core–Shell Structure as a Binder-Free Electrode for Flexible All-Solid-State Asymmetric Supercapacitors. *Nanoscale* **2020**, *12*, 1852–1863.
(35) Lv, Q.; Wu, M.; Shen, Y. Enhanced Swelling Ratio and Water Retention Capacity for Novel Super-Absorbent Hydrogel. *Colloids Surf., A* **2019**, *583*, No. 123972.
(36) Yu, X.; Luo, Z.; Ouyang, X.; Ye, H.; Liu, Y.; Jiang, X.; Xiang, L. Self-Adhesive, Self-Healing, and Water-Soluble Polymeric Dry Electrodes for Robust Physiological Signal Monitoring. *ACS Appl. Electron. Mater.* **2024**, *6*, 5201–5211.
(37) Sharma, V.; Aman, M.; Omar, S. NiMn-Layered Double Hydroxide Porous Nanoarchitectures as a Bifunctional Material for Accelerated p-Nitrophenol Reduction and Freestanding Supercapacitor Electrodes. *ACS Appl. Nano Mater.* **2022**, *5* (10), 15651–15664.
(38) Wang, Z.; Wang, H.; Wang, Y.; Wan, S.; Pei, D.; Li, K.; Lu, H. High-Performance Supercapacitor Materials Based on NiMn-LDH Layered Structures with MXene Layers. *J. Alloys Compd.* **2024**, *1008*, No. 176785.
(39) Biancolli, A. L. G.; Konovalova, A.; Santiago, E. I.; Holdcroft, S. Measuring the Ionic Conductivity of Solid Polymer Electrolyte Powders. *Int. J. Electrochem. Sci.* **2023**, *18*, No. 100288.
(40) De, S.; Cramer, C.; Schönhoff, M. Humidity Dependence of the Ionic Conductivity of Polyelectrolyte Complexes. *Macromolecules* **2011**, *44*, 8936–8943.
(41) Lv, C.; Tian, H.; Zhang, X.; Xiang, A. LF-NMR Analysis of the Water Mobility, State and Distribution in Sorbitol Plasticized Polyvinyl Alcohol Films. *Polym. Test.* **2018**, *70*, 67–72.
(42) Zuorro, A. Water Activity Prediction in Sugar and Polyol Systems using Theoretical Molecular Descriptors. *Int. J. Mol. Sci.* **2021**, *22*, No. 11044.
(43) Desuque, A. M.; Passamonti, F. J.; Chialvo, A. C. Evaluation of the Vapour Pressure of Aqueous NaCl-Sorbitol Solution and Correlation of the Water Activity on Composition and Temperature. *Fluid Ph. Equilibria* **2016**, *415*, 84–87.
(44) He, H.; Zhang, L.; Guan, X.; Cheng, H.; Liu, X.; Yu, S.; Wei, J.; Ouyang, J. Biocompatible Conductive Polymers with High Conductivity and High Stretchability. *ACS Appl. Mater. Interfaces* **2019**, *11*, 26185–26193.
(45) Jain, M.; Elmore, A. L.; Matthews, M. A.; Weidner, J. W. Thermodynamic Considerations of the Reversible Potential for the Nickel Electrode. *Electrochim. Acta* **1998**, *43*, 2649–2660.
(46) Verma, S.; Padha, B.; Arya, S. Thermoelectric-Powered Supercapacitors Based on Ni–Mn Nanowires Driven by Quadripartite Electrolyte. *ACS Appl. Energy Mater.* **2022**, *5*, 9090–9100.
(47) Tang, Y.; Liang, Z.; Jin, Y.; Gao, S.; Zou, R. Understanding and Tackling Lattice Manganese Exfoliation and Deactivation of Battery-Type NiMn-LDH in Fast Electrochemical Energy Storage. *J. Mater. Chem. A* **2021**, *9*, 23286–23295.
(48) Pan, G.; Yao, Y.; Zeng, X.; Sun, J.; Hu, J.; Sun, R.; Xu, J.-B.; Wong, C.-P. Learning from Natural Nacre: Constructing Layered Polymer Composites with High Thermal Conductivity. *ACS Appl. Mater. Interfaces* **2017**, *9* (38), 33001–33010.
(49) Wang, K.; Qin, W.; Wang, X.; Song, D.; Han, Y.; Lv, C.; Li, Z. Synergistic Enhancement of Ionic Thermoelectric Properties in Cementitious Composites via Dual-Mechanism Coupling for Building Energy Harvesting. *ACS Appl. Eng. Mater.* **2026**, *4* (2), 775–785.
(50) Yang, Y.; Xu, X.; Li, W.; Huang, Y.; Jiang, J.; He, L.; Jing, M.; Bai, Y.; Wu, T.; Fang, G. Multi-Color Materials NiMn LDH Loaded on Activated Carbon as Electrode for Electrochemical Performance Investigation. *Appl. Surf. Sci.* **2023**, *611*, No. 155562.
(51) Zhao, D.; Wang, H.; Khan, Z. U.; Chen, J. C.; Gabrielsson, R.; Jonsson, M. P.; Berggren, M.; Crispin, X. Ionic thermoelectric supercapacitors. *Energy Environ. Sci.* **2016**, *9*, 1450–1457.
(52) Meng, T.; Xuan, Y.; Zhang, X. A thermally chargeable hybrid supercapacitor with high power density for directly converting heat to electricity. *ACS Appl. Energy Mater.* **2021**, *4*, 6055–6061.

https://doi.org/10.1021/acsaem.6c02104
ACS Appl. Energy Mater. 2026, 9, 10302–10313